

Towards noiseless gravitational lensing simulations

Raul E. Angulo, Ruizhu Chen, Stefan Hilbert, Tom Abel

▶ **To cite this version:**

Raul E. Angulo, Ruizhu Chen, Stefan Hilbert, Tom Abel. Towards noiseless gravitational lensing simulations. Monthly Notices of the Royal Astronomical Society, 2014, 444, pp.2925-2937. 10.1093/mnras/stu1608 . insu-03645251

HAL Id: insu-03645251

https://insu.hal.science/insu-03645251

Submitted on 25 Apr 2022

HAL is a multi-disciplinary open access archive for the deposit and dissemination of scientific research documents, whether they are published or not. The documents may come from teaching and research institutions in France or abroad, or from public or private research centers.

L'archive ouverte pluridisciplinaire **HAL**, est destinée au dépôt et à la diffusion de documents scientifiques de niveau recherche, publiés ou non, émanant des établissements d'enseignement et de recherche français ou étrangers, des laboratoires publics ou privés.

Monthly Notices
of the
ROYAL ASTRONOMICAL SOCIETY

MNRAS **444,** 2925–2937 (2014) doi:10.1093/mnras/stu1608

Towards noiseless gravitational lensing simulations

Raul E. Angulo,[1,2]★ Ruizhu Chen,[2] Stefan Hilbert[3] and Tom Abel[2,4]

[1]*Centro de Estudios de Física del Cosmos de Aragón, Plaza San Juan 1, Planta-2, E-44001 Teruel, Spain*
[2]*Kavli Institute for Particle Astrophysics and Cosmology, Stanford University, SLAC National Accelerator Laboratory, Menlo Park, CA 94025, USA*
[3]*Max-Planck-Institute for Astrophysics, Karl-Schwarzschild-Str. 1, D-85740 Garching, Germany*
[4]*Institut Lagrange de Paris, Institut d'Astrophysique de Paris, 98 bis boulevard Arago, F-75014 Paris, France*

Accepted 2014 August 7. Received 2014 July 8; in original form 2013 September 3

ABSTRACT

The microphysical properties of the dark matter (DM) particle can, in principle, be constrained by the properties and abundance of substructures in galaxy clusters, as measured through strong gravitational lensing. Unfortunately, there is a lack of accurate theoretical predictions for the lensing signal of these substructures, mainly because of the discreteness noise inherent to *N*-body simulations. Here, we present a method, dubbed as Recursive-TCM, that is able to provide lensing predictions with an arbitrarily low discreteness noise. This solution is based on a novel way of interpreting the results of *N*-body simulations, where particles simply trace the evolution and distortion of Lagrangian phase-space volume elements. We discuss the advantages and limitations of this method compared to the widely used density estimators based on cloud-in-cells and adaptive-kernel smoothing. Applying the new method to a cluster-sized DM halo simulated in warm and cold DM scenarios, we show how the expected differences in their substructure population translate into differences in convergence and magnification maps. We anticipate that our method will provide the high-precision theoretical predictions required to interpret and fully exploit strong gravitational lensing observations.

Key words: gravitational lensing: strong – gravitational lensing: weak – methods: numerical – cosmology: theory – dark matter – large-scale structure of the Universe.

1 INTRODUCTION

Gravitational lensing has become a powerful and robust technique to explore the 'dark side' of our Universe (see Bartelmann 2010, for a recent review). In the near future, it is expected to probe the accelerated cosmic expansion and to constrain the properties of the dark matter (DM) particle.

In the weak regime, lensing by the large-scale structure of the Universe causes small distortions in the apparent shape of high-redshift galaxies and in the apparent temperature anisotropy of photons at the last scattering surface. These effects can be detected statistically by wide-field surveys (e.g CFHTLS[1] DES,[2] J-PAS,[3] *Euclid*,[4] LSST[5]), and by cosmic microwave background experiments (*Planck*,[6] SPT,[7] ACT[8]). From correlations in the distortions, one can infer the amplitude, shape and redshift evolution of the matter power spectrum – quantities sensitive to the initial density perturbations, the law of gravity and the cosmic expansion. Therefore, gravitational lensing measurements are expected to contribute significantly to our understanding of the Dark Energy and the physics of the early Universe (e.g. Huterer 2010; Marian et al. 2011; Oguri & Takada 2011; Hilbert et al. 2012; Giannantonio et al. 2012).

In the strong regime, efficient lensing configurations can produce multiple images of the same background galaxy or quasar. Each of these images is further distorted by intervening small-scale structures, thus the differences in their shape and/or flux can be used to constrain the substructure content of galaxy and cluster haloes (Mao & Schneider 1998; Metcalf & Madau 2001; Dalal & Kochanek 2002; Kochanek & Dalal 2004; Natarajan & Springel 2004; Natarajan, De Lucia & Springel 2007; Vegetti et al. 2010).

★E-mail: reangulo@gmail.com
[1] http://www.cfht.hawaii.edu/Science/CFHLS/
[2] http://www.darkenergysurvey.org/
[3] http://j-pas.org/
[4] http://sci.esa.int/euclid/
[5] http://www.lsst.org/
[6] http://www.esa.int/Our_Activities/Space_Science/Planck/
[7] http://pole.uchicago.edu/
[8] http://www.princeton.edu/act/

© 2014 The Authors
Published by Oxford University Press on behalf of the Royal Astronomical Society

Downloaded from https://academic.oup.com/mnras/article/444/3/2925/1061679 by CNRS - ISTO user on 25 April 2022

This method is, in fact, the only way of detecting substructures in distant galaxies (Vegetti et al. 2012). The amount and compactness of halo substructures depend strongly on the nature of the DM particle: colder candidates produce more and denser substructures (e.g. Klypin et al. 1999; Moore et al. 1999; Diemand, Kuhlen & Madau 2007; Springel et al. 2008); particles with larger self-interaction cross-sections produce shallower and more spherical density profiles (Meneghetti et al. 2001; Peter et al. 2013). Therefore, strong gravitational lensing can probe the microphysical properties of the DM particle and thus provide a direct test of the cold dark matter (CDM) paradigm.

In order to fully exploit gravitational lensing measurements in both strong and weak regimes, it is essential to have accurate predictions for the non-linear state of the mass distribution in the Universe. In particular, it is important to predict correctly the abundance, spatial distribution and internal properties of DM haloes and their substructure. Among the different theoretical approaches available, cosmological *N*-body simulations appear as the only robust and accurate method that meets these requirements.

Moreover, cosmological *N*-body simulations (e.g. Peebles 1971; Efstathiou & Eastwood 1981; Efstathiou et al. 1985; Springel et al. 2005; Angulo et al. 2012) are also invaluable cosmological tools: (i) They are the most reliable and precise method to follow the highly non-linear evolution of primordial density fluctuations (e.g. Kuhlen, Vogelsberger & Angulo 2012, for a recent review). (ii) They provide virtual universes with which we can test, predict and interpret astronomical observations (e.g. Overzier et al. 2013). (iii) They allow us to experiment with the laws of physics and the background cosmological model (e.g. Fontanot et al. 2012, 2013). Thus, numerical simulations not only can provide the theoretical predictions required by gravitational lensing, but they also can be particularly useful for testing analysis algorithms and for exploring the connection between lensing observations and the underlying cosmological model (Bartelmann et al. 1998; Jain, Seljak & White 2000; Vale & White 2003; Meneghetti et al. 2007; Hilbert et al. 2009).

Unfortunately, numerical simulations have a serious limitation that is inherent to the formulation of the *N*-body problem: in order to efficiently solve the Poisson−Vlasov equation, the initial cosmic density field must be represented by a set of *discrete* bodies. This discretization allows us to follow the non-linear dynamics and evolution of the DM fluid, but it introduces a small-scale noise that is very often larger than the small-scale lensing signal itself. The noise decreases on large scales and/or with better mass resolution. However, it is still comparable to the strong lensing signal from most of the substructure population, even with the highest resolution simulations to date (Xu et al. 2009; Rau, Vegetti & White 2013). In other words, the substructure lensing properties that could constrain the DM particle mass remain buried beneath the discreteness noise. Hence, current theoretical predictions are not sufficiently accurate for upcoming lensing measurements.

In this paper, we propose Recursive-TCM,[9] a method to create gravitational lensing simulations almost free of discreteness noise. Our procedure builds on a recently proposed method to solve for the collisionless dynamic of the DM fluid (Abel, Hahn & Kaehler 2012; Kaehler, Hahn & Abel 2012; Shandarin, Habib & Heitmann 2012; Angulo, Hahn & Abel 2013; Hahn, Abel & Kaehler 2013). The novel approach considers simulation particles as the vertices of Lagrangian phase-space volume elements, not mass carriers as in the usual interpretation of numerical simulations. The evolution and distortion of these volume elements is described by the Eulerian coordinates of simulation particles. Consequently, the DM density field is determined by spatially overlapping phase-space elements, which can be deposited on to a target grid using a recursive algorithm. The result is a continuous and smooth density field ideal for small-scale lensing simulations.[10]

We devote this paper to the presentation and testing of the algorithm. We start in Section 2 by describing how we compute the gravitational lensing signal of a set of simulation particles. We then apply our method to a cluster-size halo simulated in CDM and Warm-DM (WDM) cosmologies. These simulations are described in Section 3. In Section 4, we compare our method with standard density estimators, and show how the noise in the surface density and magnification maps is greatly reduced. This allows us to explore the impact of substructure on the strong lensing magnification fields for our CDM and WDM haloes. We present our conclusions and a discussion of possible future work in Section 5.

2 LENSING SIMULATIONS

We start by describing how the gravitational lensing signal of a set of simulation particles is computed, including details of our method to estimate the respective surface density maps.

2.1 Gravitational lensing

Within the plane lens approximation, the lensing distortions produced by a concentrated mass distribution can be derived from a lensing potential, $\Psi(\boldsymbol{\theta})$, (e.g. Bartelmann & Schneider 2001)

$$\Psi(\boldsymbol{\theta}) = \frac{1}{\pi}\int \mathrm{d}^2\boldsymbol{\theta}\kappa(\boldsymbol{\theta})\ln\left|\boldsymbol{\theta}-\boldsymbol{\theta}'\right|, \tag{1}$$

where $\boldsymbol{\theta} = (\theta_1, \theta_2)$ denotes an angular position on the (plane) sky, and the convergence $\kappa(\boldsymbol{\theta})$ is defined as

$$\kappa(\boldsymbol{\theta}) = \frac{\Sigma^{\rm ang}(\boldsymbol{\theta})}{\Sigma_{\rm c}^{\rm ang}}. \tag{2}$$

Here, $\Sigma^{\rm ang}(\boldsymbol{\theta})$ denotes the projected angular surface mass density of the lens mass concentration. The critical angular surface mass density is defined as

$$\Sigma_{\rm c}^{\rm ang} = \frac{\mathrm{c}^2}{4\pi\mathrm{G}}\frac{a_{\rm L} f_{\rm L} f_{\rm S}}{f_{\rm LS}}, \tag{3}$$

with the speed of light c, gravitational constant G, scale factor $a_{\rm L}$ at the redshift of the lens, and comoving angular diameter distances $f_{\rm L}$, $f_{\rm S}$ and $f_{\rm LS}$ from the observer to the lens, from the observer to the source, and between the source and the lens, respectively.

The deflection angle $\boldsymbol{\alpha}(\boldsymbol{\theta}) = (\alpha_1(\boldsymbol{\theta}), \alpha_2(\boldsymbol{\theta}))$, the complex shear $\gamma(\boldsymbol{\theta}) = \gamma_1(\boldsymbol{\theta}) + \mathrm{i}\gamma_2(\boldsymbol{\theta})$ and the magnification $\mu(\boldsymbol{\theta})$ are given by

$$\boldsymbol{\alpha}(\boldsymbol{\theta}) = (\Psi_1(\boldsymbol{\theta}), \Psi_2(\boldsymbol{\theta})), \tag{4}$$

$$\gamma(\boldsymbol{\theta}) = \frac{1}{2}\left[\Psi_{22}(\boldsymbol{\theta}) - \Psi_{11}(\boldsymbol{\theta})\right] - \mathrm{i}\Psi_{12}(\boldsymbol{\theta}), \tag{5}$$

$$\mu(\boldsymbol{\theta}) = \left\{[1-\kappa(\boldsymbol{\theta})]^2 - |\gamma(\boldsymbol{\theta})|^2\right\}^{-1}, \tag{6}$$

[9] The term Recursive-TCM abbreviates for 'Recursive deposit of Tethrahedra approximated by their Center of Mass'.

[10] The reduction of discreteness noise also helps to suppress the artificial fragmentation of filaments seen in WDM simulations (Angulo et al. 2013; Hahn et al. 2013).

Downloaded from https://academic.oup.com/mnras/article/444/3/2925/1061679 by CNRS - ISTO user on 25 April 2022

where the subscripts refer to partial derivatives with respect to one of the angular coordinates.

There are several ways of computing the lensing signal from numerical simulations (e.g. Wambsganss, Cen & Ostriker 1998; Couchman, Barber & Thomas 1999; Jain et al. 2000; Aubert, Amara & Metcalf 2007; Hilbert et al. 2009). Here, we choose one of the simplest, which consists in computing the surface density on a regular lattice and then solving for the lensing potential in Fourier space:

$$\Psi^F(\boldsymbol{\ell}) = \frac{1}{\pi}\kappa^F(\boldsymbol{\ell})\ln^F(\boldsymbol{\ell}) \tag{7}$$

$$2\pi^2\boldsymbol{\ell}^2\Psi^F(\boldsymbol{\ell}) = -\kappa^F(\boldsymbol{\ell}), \tag{8}$$

where the superscript F indicates a Fourier transform. These expressions can be readily evaluated by using fast Fourier transforms (FFT). However, this requires additional corrections, because FFT algorithms implicitly assume periodic boundary conditions, while the appropriate conditions should be vacuum boundary conditions. To suppress shear artefacts induced by periodic images of the mass distribution, generous zero padding is employed.[11] To recover the correct mean convergence [which is lost in the FFT methods due to setting $\kappa^F(\boldsymbol{\ell} = 0)$ to zero], the potential from the FFT is corrected by a term $\propto \boldsymbol{\theta}^2$. Finally, the lensing deflection, shear and magnification can be obtained by computing derivatives of Ψ either in Fourier space, or in real space by using finite difference methods (Hilbert et al. 2009).

2.2 Recursive-TCM: a new density estimator

The problem is now reduced to obtaining the surface mass density, $\Sigma(\theta)$, on a uniform grid from which the respective lensing potential can be computed. Essentially, this step consists in mapping a three-dimensional (3D) distribution of simulation particles on to a two-dimensional (2D) grid. Although it is in principle a simple task, in practice it is rather difficult to accurately carry out the mapping. Several authors have explored different projection methods and have concluded that all of them give rise to a noise field of amplitude comparable to the strong lensing signal produced by real DM substructures (Bradač et al. 2004; Li et al. 2006; Xu et al. 2009; Rau et al. 2013). This is true even for the highest mass resolution simulations of DM haloes available to date. Similarly, large-scale N-body simulations, with volumes comparable to that of future wide-field galaxy surveys, have typically a low number density of simulation particles, which adds a Poisson noise that dominates the small-scale weak lensing predictions (e.g. Jain et al. 2000; Vale & White 2003; Hilbert et al. 2009; Sato et al. 2009).

There are several proposed ways of dealing with this problem. For strong lensing, one of the most common ways is to model the smooth component of a DM halo with an analytic expression (e.g. a single isothermal sphere), and then add on top the substructure population (e.g. Xu et al. 2009). Although, it is possible to incorporate the correct density profile and the triaxiality of the DM halo, this method washes out all other higher order or more subtle features of the DM halo substructures such as streams, caustics, etc. For weak lensing, maps are often smoothed with a fixed-size kernel, which decreases the particle noise but also erases actual small-scale structure (Hilbert et al. 2009; Takahashi et al. 2011).

[11] For simplicity, we refrain from also applying a force-range cut-off.

Here we present Recursive-TCM, a mass-depositing scheme that captures a simulated density field in all its complexity by reducing drastically the noise introduced by the finite number of particles. The method extends the techniques proposed by Abel et al. (2012), Shandarin et al. (2012), Hahn et al. (2013), Kaehler et al. (2012), Angulo et al. (2013), and thus we refer to these papers for an extensive discussion of the method. The key idea is to consider simulation particles as vertices of Lagrangian phase-space tetrahedra. At any redshift, the particles indicate the current positions of these vertices. To create surface density maps, the matter represented by these tetrahedra is deposited on a target mesh using a recursive splitting scheme.

One way of interpreting our method is that it assigns to each particle a smoothing kernel whose *size and shape* are given by their Lagrangian (not Eulerian as in most smoothing methods) neighbours. In particular, this kernel is anisotropic and not even uniquely defined in an Eulerian space. We also note that our method is conceptually different to those that project a Delaunay or Voronoi tessellation built from the Eulerian particle distribution (Schaap & van de Weygaert 2000; Bradač et al. 2004).

The four main steps for a practical implementation of Recursive-TCM are:

(1) *Creating the initial tessellation*: first, we need to define a set of disjoint Lagrangian phase-space elements that fully fill the volume of a N-body simulation. In three dimensions, the most natural choice is a Delaunay tessellation of the unperturbed particle distribution. The result is a set of tetrahedra (six times more abundant than the number of particles) whose corners are given by the simulation particles.[12] The connectivity of each tetrahedron is fixed and stored (it can also be trivially recovered from the particles' ID number in case the ID is related to the position of a particle in an unperturbed lattice).

(2) *Reconstructing the evolved tessellation*: after the simulation has been evolved and the particles moved to different locations, the initial set of tetrahedra (which therefore also moved) is reconstructed using the stored connectivity. The internal density of each tetrahedron is assumed to be uniform, and the density field at any given location is simply given by all those tetrahedra that intersect the target location. We note that it is also possible to compute, at any point of space, other quantities besides the density, such as the number of streams, the velocity dispersion tensor, vorticity, etc. (Hahn et al. 2014).

(3) *Projecting the density field*: the next step is to compute the projected density field on a grid, i.e to map the tetrahedra on to a 2D regular mesh. The simplest way, called TCM by Hahn et al. (2013), is to represent each tetrahedron by a single point mass located at the centre of mass. Another option is to represent each tetrahedron by four particles, preserving the monopole and quadrupole of the parent polyhedra (Hahn et al. 2013). Here, we propose a more exact deposit, referred to as Recursive-TCM, which consists in recursively biparting each tetrahedron along its longest edge. The process continues until all the child tetrahedra are completely contained inside one grid cell, or a maximum number of levels in the recursion is

[12] Constructing the tessellation can be a computationally expensive task for state-of-the-art simulations (e.g. Pandey et al. 2013). However, this is trivial if the particle distribution is arranged in a regular lattice (as opposite to a glass-like distribution): each set of eight grid points defines a cube that is subdivided into six disjoint tetrahedra.

Downloaded from https://academic.oup.com/mnras/article/444/3/2925/1061679 by CNRS - ISTO user on 25 April 2022

reached. Then, each child tetrahedron is subsequently represented using a single particle of mass $2^{-l} m_{\rm tet}$ (where l is the recursion level and $m_{\rm tet}$ is the mass of the top tetrahedron) that is deposited using a nearest grid point assignment scheme.

(4) *Removing density biases*: over the range of scales in which the mass resolution of a given simulation is adequate to describe the evolution and distortion of Lagrangian phase-space volumes, our method provides a very reliable proxy for the density field (Abel et al. 2012). However, tetrahedron-based density calculations are biased if the distortion of an initial phase-space volume cannot be represented by linear transformations. This happens in two situations. One is at the centre of DM haloes, which have high densities and short dynamical times. As discussed in Hahn et al. (2013), this has the net effect of densities being overestimated at the halo centre, and underestimated at slightly outer regions. The second situation regards the tidal stripping of substructures, where some vertices of a given tetrahedron are stripped while others might still be attached to the substructure. This has the net effect of underestimating the mass associated with substructures and it might introduce spatially-coherent density biases along the orbit of substructures.

Fortunately, these biases in the density are small and can be identified and corrected for. Moreover, the centres of haloes are typically dominated by a stellar component (specially in galaxy-sized DM haloes, where the observational search for substructures is focused), and also are affected by baryonic processes absent in DM-only N-body simulations (such as feedback, adiabatic compression, etc). Hence, any DM-only-based predictions need to be altered to account for these and produce realistic lensing efficiencies (e.g. Xu et al. 2009), so an additional correction that remove biases of our density estimator can be easily included.

Here, we propose and use a simple way to remove density biases:

(4.1) We first compute two 2D density maps of the same simulated region, one using our method and another using a traditional (noisier) estimator.

(4.2) We then apply a correction factor to the Recursive-TCM map, defined as the average ratio between densities computed using the traditional estimator and the Recursive-TCM, in bins of Recursive-TCM densities. This aims to correct the overestimation of central densities.

(4.3) We apply an additional correction factor to account for spatially coherent, large-scale biases related to tidal stripping of substructures. This extra factor is set to the ratio of the density maps using the traditional and the Recursive-TCM estimator (after the above correction is applied), both Gaussian smoothed to keep only large-scale modes.

As we will show in the next section, this simple correction procedure eliminates most biases in surface density maps, preserving the reduced noise properties of our method. We note, however, that more sophisticated correction methods are possible and should decrease the biases even further. Some possible extensions are applying corrections to 3D densities instead of projected ones, and/or applying separate correction factors for different substructures. We also note that the Lagrangian phase-space elements we employ can be adaptively refined during the gravitational evolution of an object. In such case, we expect Recursive-TCM to be completely unbiased and thus eliminating the need of a posteriori correction. We plan to investigate this in a future work.

3 RECURSIVE-TCM IN ACTION

For illustrative purposes, we now apply our new method to numerical simulations of cold and warm DM cosmologies. We start by presenting these N-body simulations, together with one particular DM halo on which we focus our analysis. Then, we provide details of our density estimator when applied to these simulated objects.

3.1 Parent N-body runs

We employ two of the cosmological N-body calculations presented in Angulo et al. (2013). These simulate two different cosmological scenarios: (i) a standard CDM and (ii) a WDM model with a 250 eV DM particle mass. In the latter, fluctuations below $k \sim 1\,h\,{\rm Mpc}^{-1}$ are suppressed, which translates into a lack of collapsed structures below $M \sim 2 \times 10^{12}\,h^{-1}\,{\rm M}_{\odot}$, and consequently into a strong suppression of the subhalo population of massive haloes. Although this WDM model is ruled out by observations (Viel et al. 2013), we will consider it for illustrative purposes. The cosmological parameters of the simulations are consistent with those inferred from the WMAP7 data release (Komatsu et al. 2011): $\Omega_{\rm m} = 0.276$, $\Omega_{\Lambda} = 0.724$, $\Omega_{\rm b} = 0.045$, $h = 0.703$, $\sigma_8 = 0.811$ and spectral index $n_{\rm s} = 0.96$.

Each of these two simulations corresponds to a cubic region of $L = 80\,h^{-1}$ Mpc side length, containing 1024^3 simulation particles of mass $3.65 \times 10^7\,h^{-1}\,{\rm M}_{\odot}$. The initial conditions were created using the MUSIC code (Hahn & Abel 2011) at $z = 63$. The particles were subsequently evolved using a Tree-PM method, as implemented in the L-GADGET3 code (Angulo et al. 2012; Springel et al. 2005). Gravitational forces are smoothed using a Plummer-equivalent softening length set to $5\,h^{-1}$ kpc. Additionally, we have located DM haloes using an FoF algorithm (Davis et al. 1985) (using a standard value for the linking length $b = 0.2$), and identified self-bound substructures (or subhalos) within these haloes using the SUBFIND algorithm (Springel, Yoshida & White 2001).

The numerical simulations were started using identical phases and evolved with the same numerical parameters, which allows a direct comparison of structure formation in general, and of gravitational lensing signatures in particular.

3.2 Target cluster-sized DM halo

For our strong gravitational lensing analysis, we will focus on the most massive cluster present in our simulations at $z = 0$. This object has a mass of $M_{200} = 4.38 \times 10^{14}\ h^{-1}\,{\rm M}_{\odot}$, and it is resolved with more than 10 million particles. For comparison, this corresponds roughly to the lowest resolution runs of the clusters in the Phoenix project (Gao et al. 2012), and it is a factor of 10 coarser than the main cluster employed by Rau et al. (2013).[13] The force resolution is ∼250 times smaller than the halo's virial radius, and thus the halo structure is resolved adequately for our purposes.

The spherically averaged density profile of the halo is well fitted by a cored NFW profile (Navarro, Frenk & White 1996, 1997), $\rho(r)^{-1} \propto \sqrt{(r/r_{\rm s})^2 + (r_{\rm c}/r_{\rm s})^2}(1 + r/r_{\rm s})^2$, with concentration $r_{\rm s}/r_{200} = 3.9$, and core radius, $r_{\rm c} = 5\,h^{-1}$ kpc, both in CDM and WDM. We note that the core is a numerical artefact, and arises due to the lack of force resolution on scales smaller than the simulation softening length.

Fig. 1 shows an image of the selected halo in our two cosmological scenarios. The DM halo displays the same overall structure in

[13] Our force resolution is also much lower.

Downloaded from https://academic.oup.com/mnras/article/444/3/2925/1061679 by CNRS - ISTO user on 25 April 2022

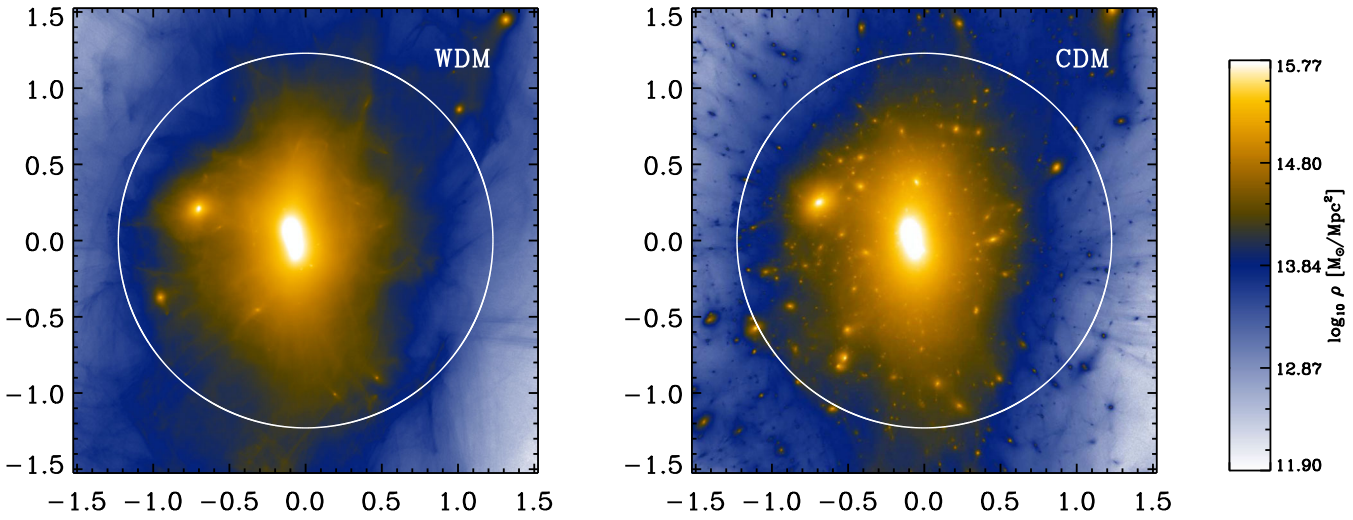


Figure 1. Projected DM density, as computed by Recursive-TCM, for the most massive halo in our simulations at $z = 0$ ($M_{200} = 4.38 \times 10^{14}\, h^{-1}\, \mathrm{M}_{\odot}$). Each image corresponds to a square region of $3.05\, h^{-1}$ Mpc side length and $3\, h^{-1}$ Mpc projection depth around the cluster centre. The white circle indicates the virial radius $R_{200} = 1.229\ h^{-1}$ Mpc. The left-hand panel shows the halo in a WDM scenario, the right-hand panel assumes a CDM cosmology.

WDM and in CDM, and the differences caused by the DM particle mass are evident only in their small-scale properties. In CDM, the halo contains a wealth of substructure: a large number of small clumps that are the remnants of previously accreted DM haloes. These, in contrast, are almost absent when WDM is adopted, but caustics, streams and filaments are instead much better defined. Inside R_{200} of the CDM halo, we find 2121 substructures with more than 15 particles, which corresponds to a minimum subhalo mass of $M_{\rm s} \geq 7.3 \times 10^8\, h^{-1}\, \mathrm{M}_{\odot}$. Contrasting this, we found only 119 substructures inside the WDM halo – which are mostly a result of numerical fragmentation of filaments (Wang, Mo & Jing 2007; Angulo et al. 2013). The substructure population contributes 1.7 and 6.5 per cent of the mass inside R_{200}, respectively, for our WDM and CDM halo.

Considering only substructure with masses above $10^{10}\, \mathrm{M}_{\odot}$, the subhalo mass function in CDM follows a power law $\mathrm{d}n/\mathrm{d}\log m_{\rm s} \propto m_{\rm s}^{-0.79}$. However, the slope decreases to -0.66 when we consider all the subhalos detected. These values are shallower that the average slope found in other simulations (-0.9, e.g. Angulo, Baugh & Lacey 2008; Gao et al. 2012). The discrepancy is most likely caused by our low force resolution compared to our mass resolution (many low-mass haloes are tidally disrupted too efficiently due to our low force resolution, which makes our subhalo mass function being incomplete up to higher subhalo masses than in simulations with smaller softening lengths), which could explain the change in slope in the subhalo mass function. Although these discrepancies are not important for our work, we caution the reader that the amount of substructure in our work is underestimated compared to other simulations of similar mass resolution.

3.3 Recursive-TCM lensing simulations

We are now in position of applying our method to the WDM and CDM halo described before. We artificially place the haloes at $z = 0.32$, where the most massive galaxy clusters are expected to be observed, and assume a background source population located at $z = 2$. We consider the 3D particle distribution inside a region of dimensions $0.6 \times 0.6\ h^{-1}$ Mpc (equal to $0.5 \times R_{200}$) and $3\ h^{-1}$ Mpc deep centred on our halo, and project it on to a 1000^2-pixels mesh. This yields a spatial resolution of $0.6\, h^{-1}$ kpc, sufficient to resolve the smallest structures present in our simulation given our gravitational resolution limit ($5\, h^{-1}$ kpc). We checked that neglecting structures beyond our projected density field is a good approximation for the lensing quantities explored in this paper: we repeated our analysis considering a four times larger region, covering $1.2 \times 1.2\, h^{-1}$ Mpc, and found no significant differences in the resulting magnification maps.

We apply our full Recursive-TCM algorithm using a maximum of 10 recursion levels, i.e. every top-level tetrahedron is split into $2^{10} = 1024$ smaller tetrahedra, at most.[14] Using these maps, we create convergence fields, compute the lensing potential, and derive the associated μ, γ and α, as described in Section 2.1. We use a $32\,768^2$ FFT mesh (this is approximately a factor of thousand larger than the density mesh to allow for non-periodic boundary conditions), and compute the spatial derivatives in Fourier space.

The computational cost of our Recursive-TCM algorithm is higher than usual projection methods, but it is still negligible compared to the time employed in carrying out an N-body simulation. For our particular data structure, data access and target grid, and maximum recursion level, it took 123 min using 256 processors, i.e. 500 CPU hours. It is important to remember that this corresponds to an implementation in software for CPUs, and that less recursion levels significantly reduce the execution time. In addition, alternative algorithms based on GPU-rendering routines can, in principle, achieve significantly better performances (Kaehler et al. 2012).

For comparison, we computed densities using two additional techniques. The first one, referred to as CiC, represents each particle by a cube of uniform density and size equal to the cell size of the target grid. This is the most-common projection method in cosmology (Hockney & Eastwood 1981). The second method, referred to as smoothed particle hydrodynamics (SPH), employs a spherically-symmetric polynomial kernel (Springel et al. 2005) to

[14] We note that the value of 10 is the maximum allowed recursion level in the deposit. In practice, unless a tetrahedron is extremely stretched, it will never reach this stage because all its child tetrahedra will be smaller than the pixel size. In this sense, the deposit algorithm automatically adapts to the mesh resolution.

Downloaded from https://academic.oup.com/mnras/article/444/3/2925/1061679 by CNRS - ISTO user on 25 April 2022

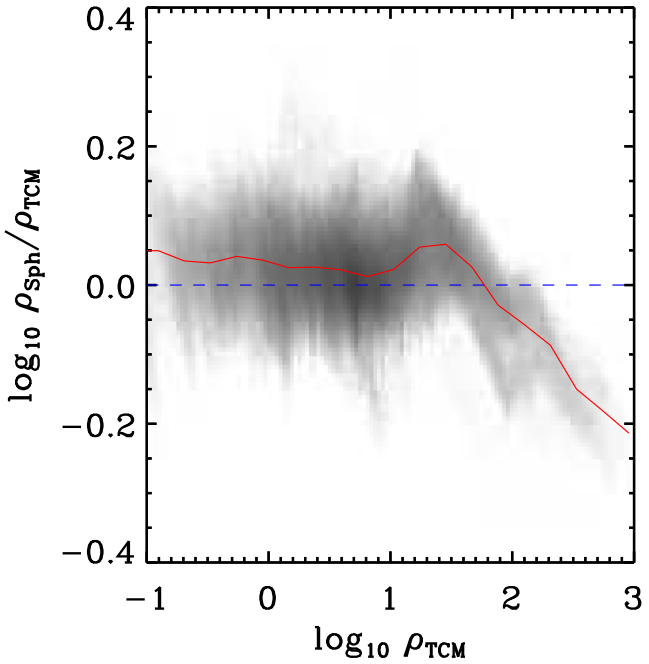


Figure 2. Relation between the densities estimated using Recursive-TCM and SPH, for 1000^2 pixels covering the inner $0.6 \times 0.6\,h^{-1}$ Mpc region centred in our WDM cluster. The red line display the mean value in logarithmic bins of $\Delta \log \rho_{\rm rtcm} = 0.1$.

project each particle on to our 2D grid. The characteristic size of the kernel is given by the local density about each particle, explicitly, by the 3D distance to the 32nd nearest neighbour. This approach is the core of the SPH (Monaghan 1992) numerical formalism.

3.4 Bias correction

As discussed in Section 2.2, Recursive-TCM densities can be biased in regions where heavy winding of the primordial phase-space sheet occurs. These biases can be seen in Figs 2 and 3, which compare results obtained using our method with those obtained using SPH. In particular, Fig. 2 shows the overestimation of the density in high-density regions (values below the unity), which in turn results into an underestimation of the density in comparatively lower density regions (values above the unity). In addition, Fig. 3 shows the large-scale coherent bias caused by the tidal stripping of substructures. These effects were explored in detail in Hahn et al. (2013). Fortunately, we can use a noisy estimator to correct for such biases, as we will show below. In practice, we follow the procedure described in §2.2 and apply a two-step bias correction.

The first step accounts for the overestimation of the density in central regions by multiplying Recursive-TCM densities by a factor that depends only on density. This factor was computed as the geometric mean of the ratio between densities estimated using SPH and Recursive-TCM, in logarithmic bins of $\Delta \log \rho_{\rm rtcm} = 0.1$, and it is shown as a red line in Fig. 2. Because the densities produced by our tetrahedral approach are biased high in central regions of DM haloes (see Section 2.2), the average ratio progressively decreases at higher densities. The largest correction factor is 0.4 at the very centre of our halo. We note that at low densities it approaches a value somewhat larger than the unity as a result of mass conservation and of the large-scale bias we discuss next.

The second correction step accounts for spatially coherent biases. In Fig. 3, we show the ratio between convergence maps in SPH and

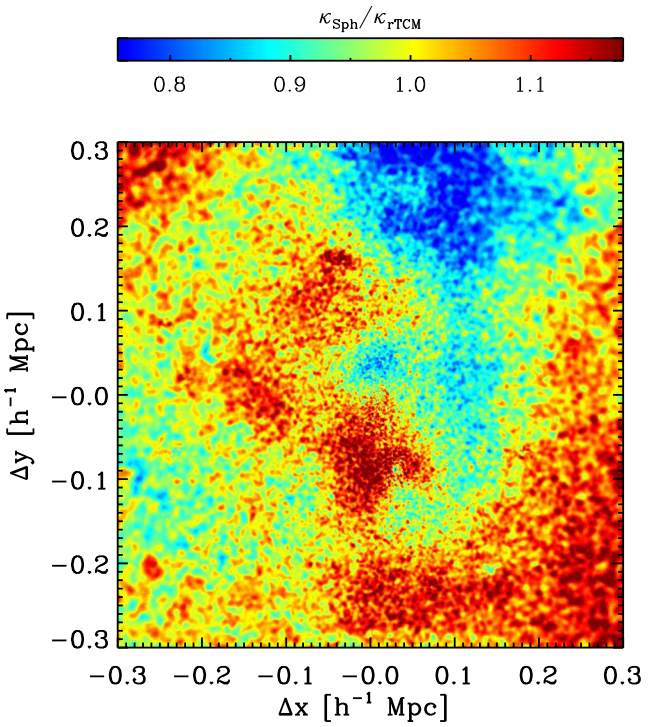


Figure 3. Fractional difference between the convergence maps built using the SPH and Recursive-TCM methods. The region displayed corresponds to the inner $0.6 \times 0.6\,h^{-1}$ Mpc region centred in our WDM halo.

in Recursive-TCM for our WDM halo and after the first correction has been applied. Ideally, this figure would be a pure white-noise field, however, we can clearly see that there is a large-scale component in this field. This arises partially because the 2D projected density field is not a one-to-one function of the full 6D phase-space structure (which determines the amount of winding and overestimation). Another aspect contributing to this map is related to mass accretion history and shortcomings of the tetrahedron-based densities to represent the tidal stripping of infalling DM haloes. In order to correct for this, we further divide the Recursive-TCM map by a version of the map shown in Fig. 3, but smoothed with a Gaussian kernel of size $50\,h^{-1}$ kpc. We note that this scale is set to be larger than those dominated by discreteness noise in SPH. As we will see later, the simple procedure described here, is successful in producing accurate lensing maps.

4 RESULTS

We now present and discuss the results of our lensing simulations. We first focus on the input surface density maps, and then on lensing magnification maps. In particular, we discuss the performance of our algorithm and the role of discreteness noise compared to the signal of DM substructures.

4.1 The surface densities and lensing convergence

Fig. 4 shows maps of the surface density in the inner regions of our WDM (top row) and CDM haloes (bottom row). Each column shows the result of one of our three projection methods, as indicated by the legend. Note that the colour scale is identical in all six panels.

In both cosmological scenarios, we can appreciate how the small-scale noise is decreased from left to right. The CiC method shows the largest fluctuations, though we note that the visual impression

Downloaded from https://academic.oup.com/mnras/article/444/3/2925/1061679 by CNRS - ISTO user on 25 April 2022

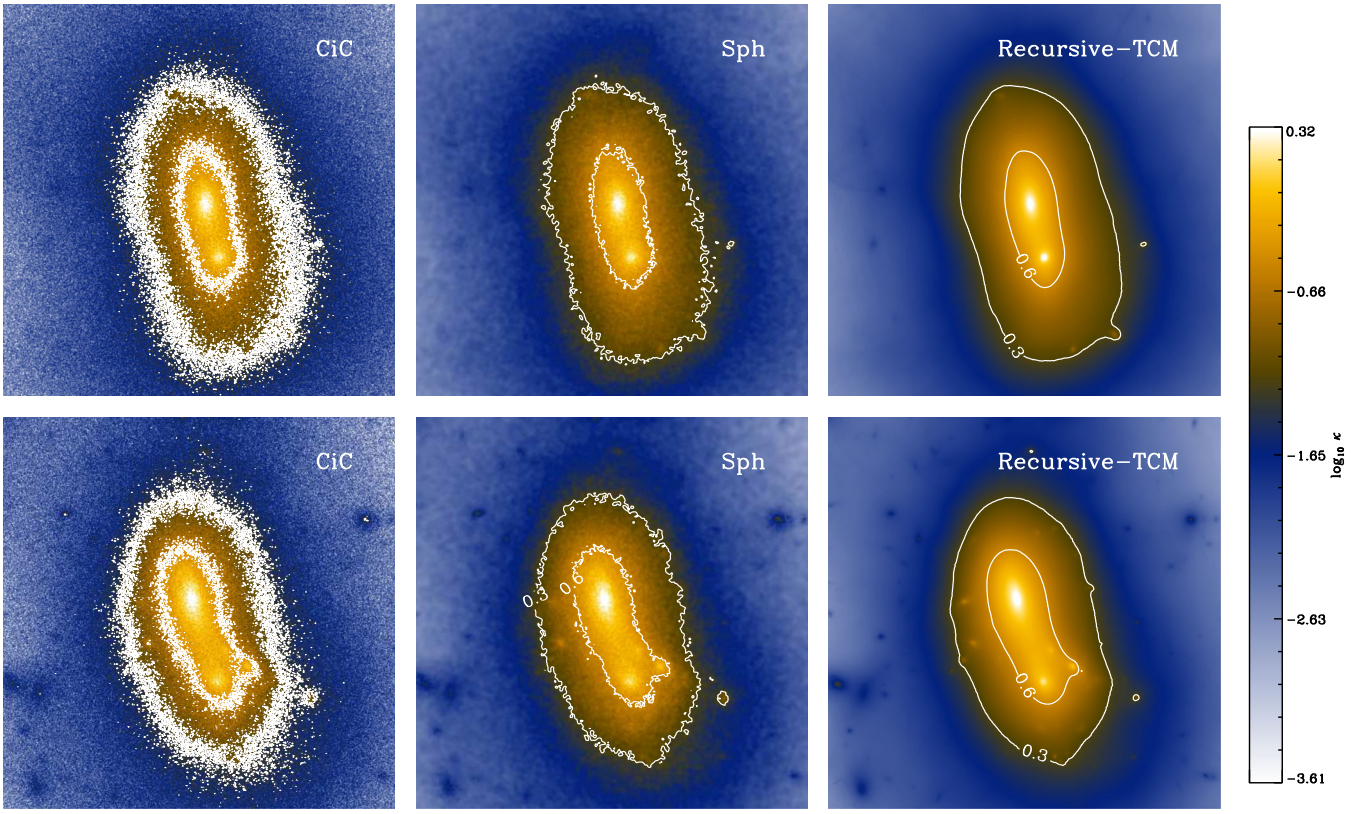


Figure 4. The convergence κ in the central $0.6 \times 0.6\,h^{-1}$ Mpc region about our WDM (top row) and CDM clusters (bottom row), using CiC, SPH, or Recursive-TCM density estimates. The colour scale is identical for all six sub-images. Note the different noise levels present in the different projection methods. Recursive-TCM displays the least noise.

of the noise depends on the target mesh resolution, as this sets the size of the CiC smoothing kernel. The SPH method reduces the noise significantly in this case, though still a considerable amount of spurious fluctuations remains. These two images illustrate the discretization-related noise in traditional density estimators.

In contrast, the new Recursive-TCM method, does not present any appreciable noise thanks to the extra sophistication in the mass deposit, nor presents appreciable biases thanks to the correction method described in Section 2.2. We note that despite being much smoother, all those peaks seen clearly in the CiC and SPH maps also appear in the Recursive-TCM maps. It is important to note that our method is the only one that could in principle distinguish random fluctuations in surface density maps from those produced by halo substructures: compare the differences between the CDM and WDM halo in rightmost column, with the differences seen in the leftmost column. In both CiC and SPH, it is almost impossible to visually distinguish CDM from WDM.

We now carry out several tests of the algorithm as applied to our WDM halo. We chose WDM over CDM since the former allows a more straightforward comparison among different methods and resolutions. The reason for this is that in WDM there is no small-scale structure, thus exactly the same mass distribution is represented at all resolutions. This is not the case in CDM since there is always structure at the resolution limit of a simulation.

Fig. 5 shows the power spectrum of the surface overdensity, $\delta = \Sigma/\langle\Sigma\rangle - 1$, as given by the three projection methods applied to the WDM halo. We note that the measurements are robust only until $k \sim 0.4 \times k_{\rm nyq}$, where $k_{\rm nyq} = 1000/(0.6\,h^{-1}\,{\rm Mpc}) \times \pi = 5235\,h\,{\rm Mpc}^{-1}$ denotes the Nyquist frequency of the surface density

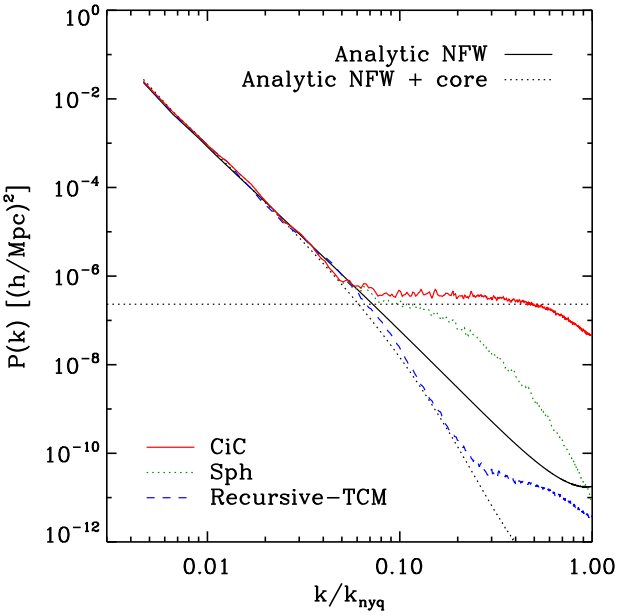


Figure 5. The power spectra of the 2D overdensity $\delta = \Sigma/\langle\Sigma\rangle - 1$, produced by the three projection algorithms when applied to a WDM halo. Wavelengths are shown in units of the Nyquist frequency of the density mesh $k_{\rm nyq} = 5235\,h\,{\rm Mpc}^{-1}$. The method proposed here, Recursive-TCM, yields the lowest amplitude on small-scale fluctuations. Also shown are expectations for a smooth NFW profile without and with central core. The dotted horizontal line indicates the white-noise level.

Downloaded from https://academic.oup.com/mnras/article/444/3/2925/1061679 by CNRS - ISTO user on 25 April 2022

mesh. On smaller scales, aliasing and the mass assignment window introduce visible artefacts, damping the measured power spectra. We also display the expectations of a white-noise field with the same number of point particles as those projected in our surface density maps. For comparison, we also show the expectations for a (cored) NFW halo with the same mass and concentration as the spherically-averaged density profile of our DM haloes, but without noise.

Comparing all the measured power spectra, we observe a situation consistent with the visual impression provided before. On large and intermediate scales, all methods provide essentially identical power spectra decreasing as k^{-4}, as expected for an NFW profile. This incidentally supports the validity of our simple approach to correct the biases in Recursive-TCM densities.

On scales smaller than $k \gtrsim 20\ h\,\mathrm{Mpc}^{-1}$ or roughly $r \sim 50\ h^{-1}$ kpc ($k > 0.08 \times k_{\rm nyq}$) – a scale much larger than the typical size of substructures – all methods begin to differ. The CiC spectrum follows the value expected for a 2D Poisson field: $P_{\rm noise} = n^{-1} = 2.3 \times 10^{-7}$. Interestingly, the SPH method levels to this expectation at roughly the same scale as the CiC spectrum, but then decays much more quickly. This is because the SPH method heavily smooths the field on scales smaller than the kernel size. This smoothing also erases true (specially anisotropic) small-scale density fluctuations present in our DM haloes. For instance, it can be trivially seen that structures resolved with less than 32 particles will be smoothed out.

The performance of Recursive-TCM appears to be considerably better. The noise level is a few orders of magnitude below that of the other projection methods. The noise measurements are consistent with our expectations of reducing the noise in a way proportional to the maximum level of recursion, l_{max}, in the adaptive mass deposit: $P_{\rm noise} = n^{-1} \times 6 \times 2^{l_{\rm max}}$, where n is the number density of bodies used in the map creation. The prefactor of six is understood in terms of the six times more particles (one per tetrahedron) employed to describe the mass field. This scaling predicts the Poisson noise in our measurements to be a factor of $6 \times 2^{10} = 6144$ smaller than the CiC method. This value is very close to the actual differences (measured at $k = 0.27\,h\,\mathrm{Mpc}^{-1}$): 7136.7.

Finally, we can see that Recursive-TCM creates a projected mass power spectrum that is very close to that of an ideal NFW halo, differing only on the slope at high wavenumbers. On these scales, the core introduced by the softening length in our simulations becomes relevant, and the Recursive-TCM power spectrum follows that of a cored NFW profile.

4.2 Mass resolution dependence

We now explore how the noise of our convergence maps varies with the mass resolution of the underlying N-body simulation. For this, we have down-sampled the field by factors of 2, 4 and 8 in each coordinate, or equivalently, reducing the total number of particles in our N-body simulations by factors of 8, 64 and 512. The most down-sampled case is equivalent to a 128^3 particle simulation, where our WDM halo would be resolved with only 20 000 particles. For each case, we have created convergence maps with maximum recursion levels set at 2 for the original maps, and to 5, 8 and 11, respectively, for the down-sampled versions. The increased recursion level compensates the sparser particle data, so that in all four cases the maps are created with roughly the same number of tetrahedra (i.e. keeping $n^{-1} \times 2^{l_{\rm max}}$ constant).

In Fig. 6, we show the four resulting convergence maps. In all sub-panels, we see that our method produces extremely smooth surface density maps. Naturally, as we decrease the effective resolution, small-scale features slowly disappear, for instance, the three substructures located on the bottom-right side of the image. With low mass resolution, orbits and accretion become discrete and subtle radial features appear. However, even in the lower-right case, which contains almost three orders of magnitude less particles than in our original simulation, the small-scale noise is considerably smaller than with the CiC method (compare to the leftmost panel of the top row in Fig. 4). This shows that the limitation of our maps is in the actual amount of structure that the parent N-body simulation tracks correctly, and not in the discreteness noise associated with the finite number of particles.

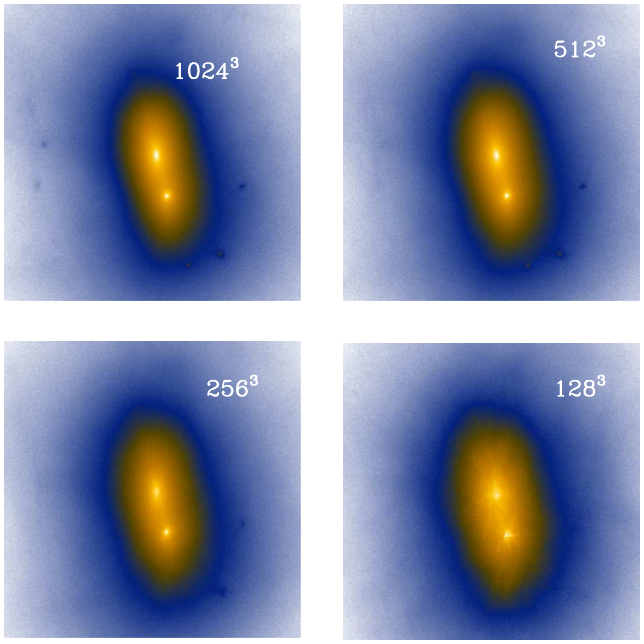


Figure 6. Comparison of the convergence maps created by the same particle distribution of the WDM halo down-sampled by factors of 8 (top right), 64 (bottom left) or 512 (bottom right). Therefore, these would correspond to haloes simulated with 1024^3, 512^3, 256^3 and 128^3, respectively, as indicated by the legend. The original map is shown on the top-left panel. We use an identical logarithmic colour scale in all subpanels.

A quantitative comparison can be obtained from Fig. 7, which shows the 2D power spectra of our four test cases, with and without applying our density correction (cf. Section 3.4). The overall shape of the power spectra is very similar among all resolutions, as expected from the previous images, but small differences arise due to the different amount of structure resolved in the different cases. Nevertheless, the discreteness noise appears at the same level and is set by the maximum amount of deposited tetrahedra. This again shows that the limitation of our gravitational lensing simulations mostly resides on the ability of the parent N-body simulation to represent DM structures properly, and not in an artificial noise introduced by our mass-projection method. In the next subsection, we will show that this has positive repercussions on simulated lensing signals.

4.3 The lensing magnification

The magnification field, $\mu(\boldsymbol{x})$, which gives the ratio of the area of the lensed image to the original area of the source, depends on second-order derivatives of the lensing potential (whereas $\alpha((\boldsymbol{x}))$ depends

Downloaded from https://academic.oup.com/mnras/article/444/3/2925/1061679 by CNRS - ISTO user on 25 April 2022

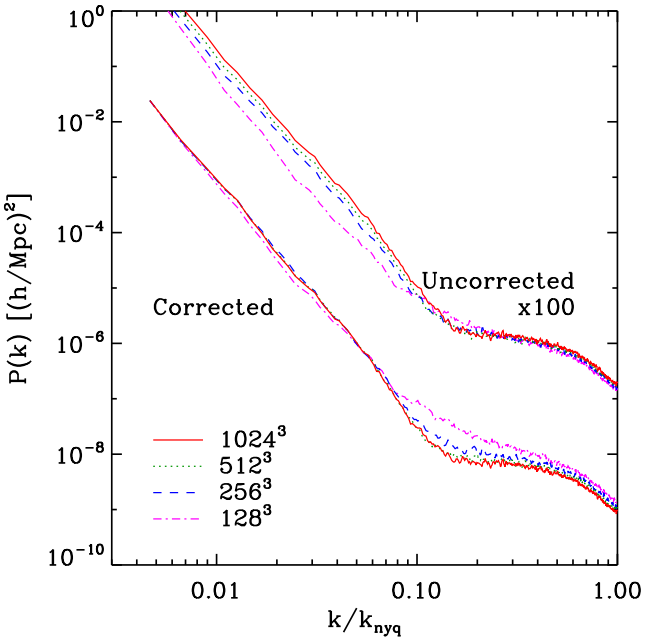


Figure 7. Comparison between the power spectra of projected overdensity maps created from the WDM halo with the Recursive-TCM method applied on progressively sparser data. The solid red line show the result for our original data set and a maximum level of recursion set to 4, whereas the dot–dashed magenta line shows the result for a case using 512 less particles but allowing seven further levels of refinements.

only on first-order derivatives). Thus, $\mu((\boldsymbol{x}))$ is very sensitive to small perturbations to the lensing potential (such as those caused by subhalos). This is also the reason why $\mu((\boldsymbol{x}))$ is very sensitive to the noise introduced by the discretization in *N*-body simulations.

In Fig. 8, we display maps of the inverse of the magnification field, $\mu^{-1}((\boldsymbol{x}))$, created from each of the three projection methods we consider. We highlight two contour lines: (i) where the magnification is formally infinite, $\mu^{-1} = 0$, which are known as critical lines; and (ii) where $\mu^{-1} = 0.6$, which serves as an eye guide for the amount of noise and substructures in the outer parts of the halo. Note that our simulated cluster is not a particularly efficient lens, partly due to its particular dynamical state, and also because of our modest force resolution and the lack of a modelling of a central stellar component.

While the magnification maps from CiC, SPH and Recursive-TCM agree on large scales, they differ substantially in the amount of associated small-scale noise. In the CiC case, the noise fluctuations make it almost impossible to distinguish CDM from WDM based solely on the topology of iso-μ lines. The same is true to some degree for SPH. The method Recursive-TCM is superior: the contours are not disturbed by discreteness noise, which allows us to explore the magnification field with great detail. When applied to the WDM case, we see contour lines that are extremely smooth. For the CDM halo, the contour lines are also very smooth in most parts of the map, but they display many small protuberances with high significance. As we will see in the next section, these are caused by the rich substructure population of this halo and thus are a distinctive signature of the DM candidate properties.

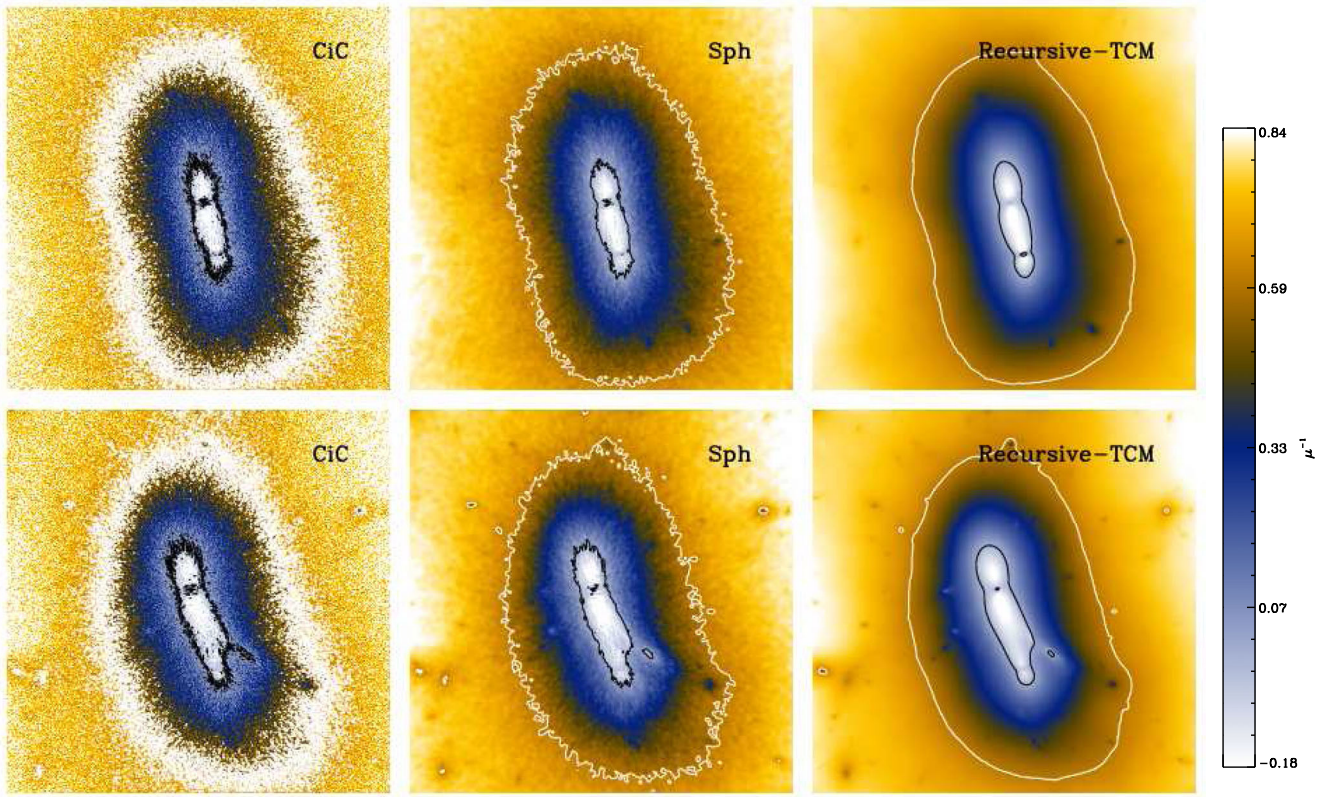


Figure 8. Map of the inverse of the magnification field, μ^{-1}, at the central region of our WDM (top) and CDM (bottom). The region displayed matches that shown in Fig. 4. White and black lines shows contours, where $\mu^{-1} = 0.6$ and 0, respectively. Note we use the same colour scale in all panels, ranging from −0.18 (white) to 0.85 (light yellow).

Downloaded from https://academic.oup.com/mnras/article/444/3/2925/1061679 by CNRS - ISTO user on 25 April 2022

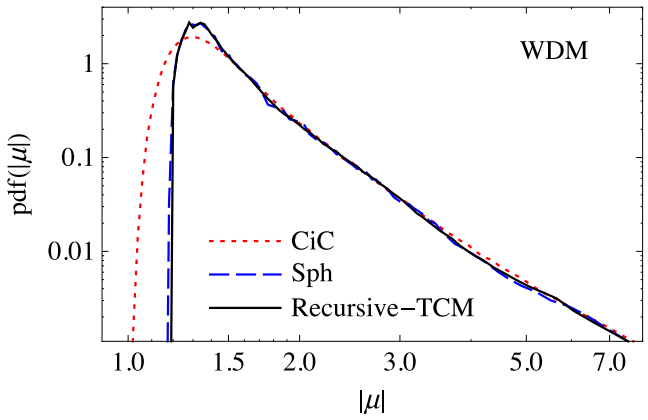


Figure 9. Probability density pdf($|\mu|$) of the magnification modulus $|\mu|$ computed with CiC (red dotted), SPH (blue dashed), and Recursive-TCM (black solid lines) for the WDM halo.

Fig. 9 shows frequency of magnification values predicted by the different methods for the WDM halo (results for the CDM halo are very similar). The noise in the CiC magnification maps leads to substantially broader magnification distributions compared to those for SPH and Recursive-TCM. In contrast, the distributions predicted by SPH and Recursive-TCM are very similar. However, the probability densities predicted by SPH display more features, i.e. local deviations from a smooth density function, which we attribute to residual noise in the SPH maps. This illustrates that the inferred magnification distribution at low and intermediate values is indeed different for different projection methods, even for the same simulated object.

4.4 The impact of substructures

In order to further explore the capabilities of our method, we now focus on the impact of halo substructure on the magnification and convergence maps. In Fig. 10, we show isomagnification lines, as computed in Recursive-TCM maps, together with the substructures identified with more than 50 particles in our simulated halo. Note that the small amount of noise visible in the outer contour is a result of the maximum number of recursion levels ($l_{\rm max} = 10$) employed in our method. This noise can also be seen in the power spectra of the projected density field shown in Fig. 5, and, as we discussed earlier, it can be reduced further by simply increasing $l_{\rm max}$ at the expense of more CPU time.

We can clearly see the differences between CDM and WDM. In the WDM case, there are only 13 substructures in the field, and consequently iso-μ lines are mostly smooth, showing only a few notorious protuberances. In contrast, in the CDM case, there are 89 substructures, and the iso-μ lines show many protuberances, but are almost smooth otherwise.

As Fig. 10 illustrates, all protuberances in the isomagnification contours are associated with nearby substructures. However, the relation is not simple, and different substructures produce perturbations of different importance. Moreover, in some cases fluctuations are not caused by a single substructure, but by a group of them. This case is seen, for example, in the lower-right section of the CDM $\mu^{-1} = 0.2$. In contrast, some substructures near contours do not strongly perturb the magnification field. These objects have typically surface mass densities below average. For instance, the substructure located at $(-0.04, 0.05)$ in the WDM case, has a projected density a factor of ten smaller than the substructure found at $(0.14, -0.2)$.

In Fig. 11, we compare the signal of identified substructures among the convergence maps. The x-axis shows the true subhalo mass $M_{\rm sub}$, as defined by the SUBFIND algorithm. The y-axis shows the ratio of the excess convergence $\Delta\kappa$ with respect to a simple expectation $\kappa_{\rm sub}$ based on the substructures properties. The measured value, $\Delta\kappa$, is defined as $\kappa_{\rm hm} - \kappa_{\rm back}$, where $\kappa_{\rm hm}$ is the mean convergence within the half-mass radius $R_{\rm hm}$, and the background convergence $\kappa_{\rm back}$ is the given by the mean convergence in an

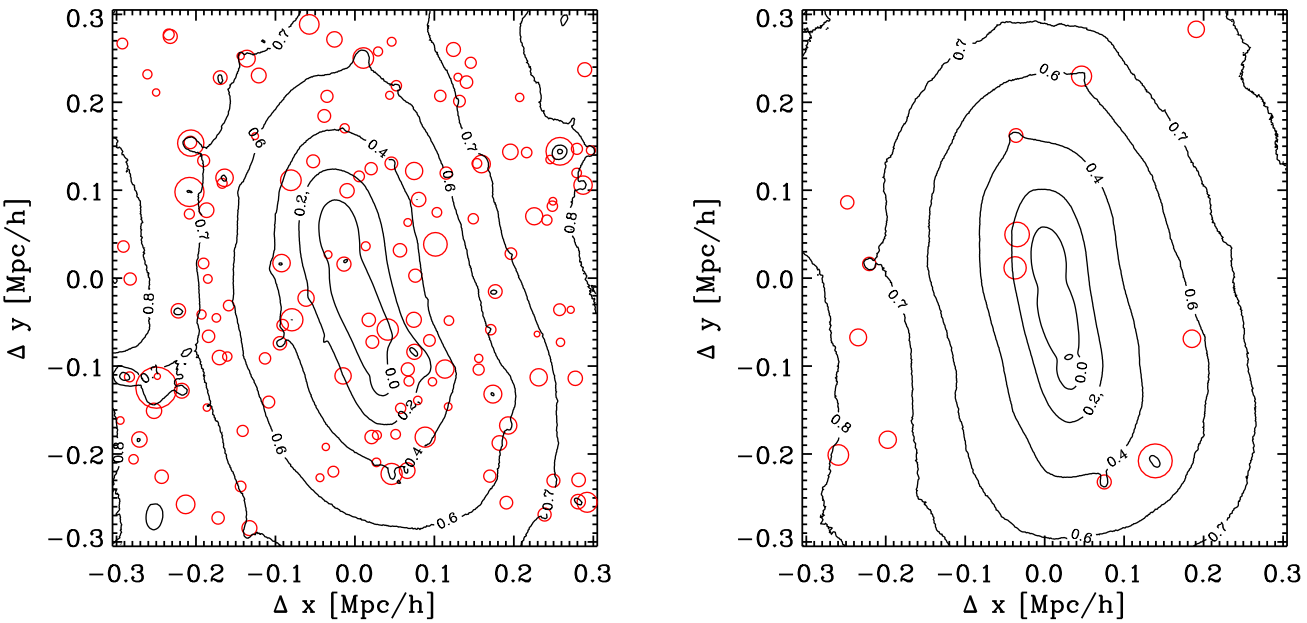


Figure 10. The relation between substructure and perturbations in lensing magnification for our simulated CDM (left) and WDM (right) halo. Black lines denote isomagnification contours at $\mu^{-1} = 0.8$, 0.7, 0.6, 0.4, 0.2 and 0 inwards. Red circles indicate the positions where substructures were identified, and their radii are equal to the half-mass radius of the respective subhalo. Note the reduced number of substructures in the WDM case, which result from the initial suppression of small-scale fluctuations.

Downloaded from https://academic.oup.com/mnras/article/444/3/2925/1061679 by CNRS - ISTO user on 25 April 2022

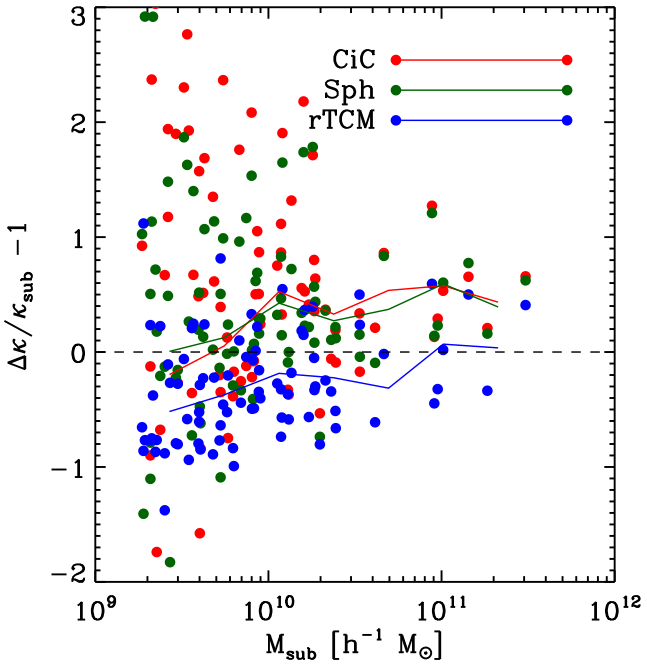


Figure 11. Ratio of the measured excess convergence $\Delta\kappa$ of substructures and a simple expectation κ_{sub}, as a function of the subhalo mass, M_{sub}, in maps constructed using the CiC, SPH and Recursive-TCM. Solid lines show the median values in seven logarithmic bins in M_{sub}.

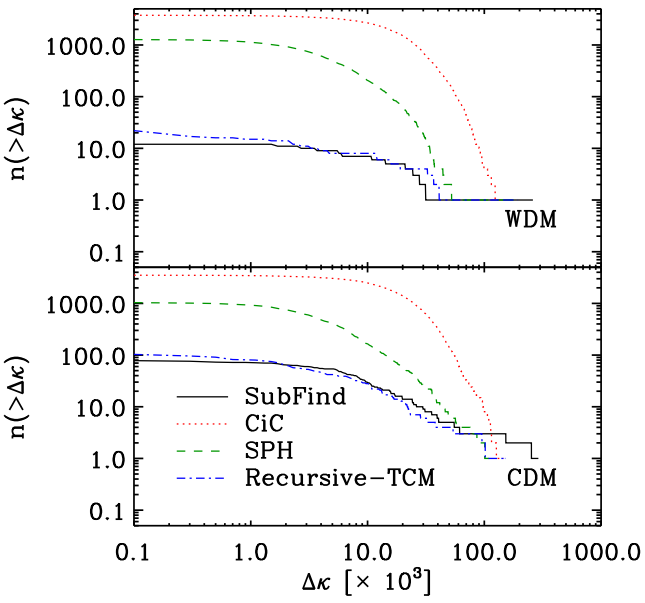


Figure 12. The cumulative number of local peaks in convergence maps detected in our WDM (top) and CDM (bottom) cluster-sized halo. In each case, we show the results for a map created using three density projection methods: CiC (red lines), SPH (green line) and Recursive-TCM blue line. In addition, we show the abundance of substructures detected in 3D by the SUBFIND algorithm.

annulus with $1.5R_{hm} < R < 1.7R_{hm}$. The expected value, κ_{sub}, is defined as $0.5M_{sub}/(\pi R_{hm}^2)/\Sigma_c$.

There are three points illustrated by this figure. The first one is that the magnification associated with substructures is actually very close to the expectations. Small deviations from unity are caused by projections effects, triaxiality or inaccuracies in the background estimation. The second point is that the scatter in $\Delta\kappa/\kappa_{sub}$ is much smaller in Recursive-TCM than in the other methods. This is thanks to a less noisy estimation of both the signal itself and the background. The third and final point is to illustrate a limitation of our method. The average value of $\Delta\kappa$ is roughly a factor of two smaller in Recursive-TCM than in the other two methods. The discrepancy is originated by two factors. First, it is due to an overestimation of the bias correction factor: since this factor is essentially set by the background halo, it does not capture the exact density biases for substructures, which have different central densities and dynamical times. The second aspect is an intrinsic underestimation of the mass associated with subhalos in Recursive-TCM. This has an origin in tetrahedra being stretched along a subhalo's orbit by tidal stripping. We estimated this effect to cause an underestimation of about 30 per cent in the mass inside subhalos for resolved substructures in our CDM halo. It remains to be explored whether more sophisticated correction procedures, or modifications to the Recursive-TCM algorithm, will alleviate these discrepancies.

In order to quantify the performance of Recursive-TCM concerning substructure lensing signals, we have implemented a hierarchical peak finder algorithm. This proceeds as follows: we start by smoothing the convergence field with a Gaussian kernel of size $r_s = 100\,h^{-1}$ kpc and then identify local peaks in the smoothed field. Then, we progressively reduce the kernel size and search for new peaks, discarding those that are inside a larger peak. We repeat this procedure for 20 different scales, uniformly spaced in $\log r_s$, down to $r_s = 1\,h^{-1}$ kpc. Finally, we compute the signal associated with each peak as $\Delta\kappa = \kappa_{rs} - \kappa_{back}$, where κ_{rs} is the average convergence within r_s and κ_{back} is the local background value defined as the average of the map in an annulus of $1.5r_s < r < 1.7r_s$.

The results are shown in Fig. 12, which displays the cumulative number of peaks detected by our algorithm when applied to CiC, SPH and Recursive-TCM maps, as a function of their local convergence excess $\Delta\kappa$. In addition, we plot as a black line the substructures detected in 3D by SUBFIND, which should correspond to gravitationally bound density peaks and that we consider as the true substructure population. The associated $\Delta\kappa$ is computed in the same way as that of our peaks, but using R_{hm} as the peak scale. Our algorithm finds 4241 (CiC), 1116 (SPH) and 125 (Recursive-TCM) peaks in the CDM map, and 4477 (CiC), 1356 (SPH) and 29 (Recursive-TCM) peaks in the WDM map.

It is clear that the CiC and SPH maps contain a large amount of spurious peaks produced by the discreteness noise. At all $\Delta\kappa$ there are between one and two orders of magnitude more detected peaks than real substructures. Moreover, the number of detected peaks is almost identical between CDM and WDM, even though the actual amount of substructure is very different. This further exemplifies that in current lensing simulations the impact of noise is comparable or larger than that of real DM substructures.

In contrast, our method recovers roughly the correct amount of peaks, which is an order of magnitude larger in CDM than in WDM. Furthermore, 59 and 69 per cent of the substructures can be matched to a peak in CDM and WDM, respectively. Among those substructures not detected as peaks, we mostly find objects with a negative or very small $\Delta\kappa$ value, which are also not detected in the CiC or SPH. This suggests that these might indeed be the false-positives in SUBFIND or special cases of projection effects. However, it might also be a consequence of the simplicity of our peak detection algorithm. In order to quantify the implications for observational constraints, this issue requires further study considering realistic input signals and analysis procedures, and perhaps more sophisticated procedures to correct for Recursive-TCM biases.

Downloaded from https://academic.oup.com/mnras/article/444/3/2925/1061679 by CNRS - ISTO user on 25 April 2022

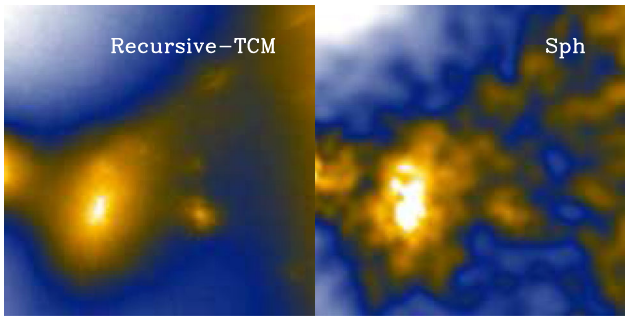


Figure 13. Zoom into a $100 \times 100\,h^{-1}$ kpc region, centred at $(\Delta x, \Delta y) = (-0.23, -0.11)\,h^{-1}$ Mpc relative to the main halo, showing the convergence field associated with a tidal feature. The left-hand panel shows a map computed using a Recursive-TCM projection method, whereas the right-hand panel shows one computed using the SPH method.

There are also peaks in the convergence maps that are not related to any identified 3D substructure. In many cases, these are due to our 3D substructure finder algorithm: a density peak not found by SUBFIND, one that fell below our mass-resolution, or one that is not a self-bound object. For instance, the large peak located at $(-0.27, -0.28)$ is not associated with any object in the respective SUBFIND catalogue. An object of a different nature is shown in Fig. 13. It does not correspond to a self-bound spherical overdensity, but to a DM stream of a tidally disrupted substructure. Such features are expected in hierarchical structure formation scenarios, and perhaps they could be eventually detected through their lensing signal. (Note that this feature is barely distinguished over the noise in SPH). For the moment, this detection serves as a further example of the potential accuracy and precision of the lensing maps created by the method presented and discussed here.

5 CONCLUSIONS

The next generation of gravitational lensing observations might help us to decipher the mysteries of the Dark Universe: Dark Energy and Dark Matter. However, high-precision theoretical predictions are essential to ensure the correct interpretation of future data sets.

In this paper, we presented Recursive-TCM, a method aimed at predicting the lensing signal from cosmological simulations with extremely high accuracy. This algorithm originates from a novel way of interpreting the results of *N*-body simulations and overcomes one of the most serious limitations of current lensing simulations: the noise introduced by the discrete nature of the particle representation of the density field.

We applied Recursive-TCM to cluster sized-haloes simulated in WDM and CDM universes. We showed that the method produces convergence maps with a noise several orders of magnitude smaller than that of traditional methods (explicitly, a factor of $\sim$7000 smaller than the formal shot-noise limit). We also showed that the method recovers the underlying power spectrum of fluctuations well below the particle shot noise of the simulations.

With traditional projection methods, the discreteness noise in lensing maps are comparable to the signal produced by DM substructure. This is not true for Recursive-TCM, where the features associated with real overdensities are preserved, but the discreteness noise is greatly reduced. We also showed that there are density biases associated with Recursive-TCM, which, however, can be mostly eliminated by a simple correction procedure. Therefore, this method is well suited for creating high-precision predictions for the relation between the underlying cosmological model and the expected signatures of small-scale structure in strong gravitational lensing observations.

With Recursive-TCM, we were able to clearly show the differences in the lensing properties between CDM and WDM. The differences come mainly from their substructure population, and thus lensing might be able to constrain the DM particle mass. However, we found that the relation between substructures and the associated lensing effects is not trivial: some substructures do not affect the convergence noticeably; many lensing perturbations are caused by more than a single structure; and a few perturbations are not associated with any self-bound substructure, but, e.g. with a tidal debris. This suggests that in order to interpret correctly the lensing measurements of substructures, a rigorous study of the detectability of substructures needs to be carried out.

In this paper, we have shown the feasibility of Recursive-TCM, providing examples of its potential when applied to a rather modest simulation. In the future, we expect our method to enable many detailed theoretical studies, exploiting state-of-the-art simulations of much higher force and mass resolution, also simulating more realistic WDM scenarios, and even taking advantage of hydrodynamical simulations. We also expect Recursive-TCM to be very useful for creating large-scale weak lensing shear and magnification maps with high fidelity and low particle noise. Moreover, the method will be crucial for testing and characterizing the performance of algorithms that extract substructure information from observed lensed galaxies, in particular methods for constraining the DM particle mass from image perturbations or flux-ratio anomalies in multiple-image systems. All this together will allow us to understand better the impact of the underlying cosmological model in lensing observations, and therefore help to unleash the full potential of gravitational lensing.

ACKNOWLEDGEMENTS

We warmly thank Oliver Hahn and Ralf Kaehler for many enlightening discussions. We also thank Simon White for valuable suggestions that improved our paper. We acknowledge useful comments on the manuscript from Carlo Giocoli, Yashar Hezaveh, Phil Marshal, Ben Metcalf, Stefan Rau and Simona Vegetti. TA gratefully acknowledges support by the National Science foundation through award number AST-0808398 and the LDRD program at the SLAC National Accelerator Laboratory as well as the Terman Fellowship at Stanford University. We gratefully acknowledge the support of Stuart Marshall and the SLAC computational team, as well as the computational resources at SLAC. Parts of the computations were carried out at the Rechenzentrum Garching (RZG) of the Max Planck Society.

REFERENCES

Abel T., Hahn O., Kaehler R., 2012, MNRAS, 427, 61
Angulo R. E., Baugh C. M., Lacey C. G., 2008, MNRAS, 387, 921
Angulo R. E., Springel V., White S. D. M., Jenkins A., Baugh C. M., Frenk C. S., 2012, MNRAS, 426, 2046
Angulo R. E., Hahn O., Abel T., 2013, MNRAS, 434, 3337
Aubert D., Amara A., Metcalf R. B., 2007, MNRAS, 376, 113
Bartelmann M., 2010, Class. Quantum Gravity, 27, 233001
Bartelmann M., Schneider P., 2001, Phys. Rep., 340, 291
Bartelmann M., Huss A., Colberg J. M., Jenkins A., Pearce F. R., 1998, A&A, 330, 1
Bradač M., Schneider P., Lombardi M., Steinmetz M., Koopmans L. V. E., Navarro J. F., 2004, A&A, 423, 797

Downloaded from https://academic.oup.com/mnras/article/444/3/2925/1061679 by CNRS - ISTO user on 25 April 2022

Couchman H. M. P., Barber A. J., Thomas P. A., 1999, MNRAS, 308, 180
Dalal N., Kochanek C. S., 2002, ApJ, 572, 25
Davis M., Efstathiou G., Frenk C. S., White S. D. M., 1985, ApJ, 292, 371
Diemand J., Kuhlen M., Madau P., 2007, ApJ, 667, 859
Efstathiou G., Eastwood J. W., 1981, MNRAS, 194, 503
Efstathiou G., Davis M., White S. D. M., Frenk C. S., 1985, ApJS, 57, 241
Fontanot F., Springel V., Angulo R. E., Henriques B., 2012, MNRAS, 426, 2335
Fontanot F., Puchwein E., Springel V., Bianchi D., 2013, MNRAS, 436, 2672
Gao L., Navarro J. F., Frenk C. S., Jenkins A., Springel V., White S. D. M., 2012, MNRAS, 425, 2169
Giannantonio T., Porciani C., Carron J., Amara A., Pillepich A., 2012, MNRAS, 422, 2854
Hahn O., Abel T., 2011, MNRAS, 415, 2101
Hahn O., Abel T., Kaehler R., 2013, MNRAS, 434, 1171
Hahn O., Angulo R. E., Abel T., 2014, preprint (arXiv:1404.2280)
Hilbert S., Hartlap J., White S. D. M., Schneider P., 2009, A&A, 499, 31
Hilbert S., Marian L., Smith R. E., Desjacques V., 2012, MNRAS, 426, 2870
Hockney R. W., Eastwood J. W., 1981, Computer Simulation Using Particles. McGraw-Hill, New York
Huterer D., 2010, Gen. Relativ. Gravit., 42, 2177
Jain B., Seljak U., White S., 2000, ApJ, 530, 547
Kaehler R., Hahn O., Abel T., 2012, preprint (arXiv:1208.3206)
Klypin A., Kravtsov A. V., Valenzuela O., Prada F., 1999, ApJ, 522, 82
Kochanek C. S., Dalal N., 2004, ApJ, 610, 69
Komatsu E. et al., 2011, ApJS, 192, 18
Kuhlen M., Vogelsberger M., Angulo R., 2012, Phys. Dark Univ., 1, 50
Li G.-L., Mao S., Jing Y. P., Kang X., Bartelmann M., 2006, ApJ, 652, 43
Mao S., Schneider P., 1998, MNRAS, 295, 587
Marian L., Hilbert S., Smith R. E., Schneider P., Desjacques V., 2011, ApJ, 728, L13
Meneghetti M., Yoshida N., Bartelmann M., Moscardini L., Springel V., Tormen G., White S. D. M., 2001, MNRAS, 325, 435
Meneghetti M., Argazzi R., Pace F., Moscardini L., Dolag K., Bartelmann M., Li G., Oguri M., 2007, A&A, 461, 25
Metcalf R. B., Madau P., 2001, ApJ, 563, 9
Monaghan J. J., 1992, ARA&A, 30, 543
Moore B., Ghigna S., Governato F., Lake G., Quinn T., Stadel J., Tozzi P., 1999, ApJ, 524, L19
Natarajan P., Springel V., 2004, ApJ, 617, L13
Natarajan P., De Lucia G., Springel V., 2007, MNRAS, 376, 180
Navarro J. F., Frenk C. S., White S. D. M., 1996, ApJ, 462, 563
Navarro J. F., Frenk C. S., White S. D. M., 1997, ApJ, 490, 493
Oguri M., Takada M., 2011, Phys. Rev. D, 83, 023008
Overzier R., Lemson G., Angulo R. E., Bertin E., Blaizot J., Henriques B. M. B., Marleau G.-D., White S. D. M., 2013, MNRAS, 428, 778
Pandey B., White S. D. M., Springel V., Angulo R. E., 2013, MNRAS, 435, 2968
Peebles P. J. E., 1971, A&A, 11, 377
Peter A. H. G., Rocha M., Bullock J. S., Kaplinghat M., 2013, MNRAS, 430, 105
Rau S., Vegetti S., White S. D. M., 2013, MNRAS, 430, 2232
Sato M., Hamana T., Takahashi R., Takada M., Yoshida N., Matsubara T., Sugiyama N., 2009, ApJ, 701, 945
Schaap W. E., van de Weygaert R., 2000, A&A, 363, L29
Shandarin S., Habib S., Heitmann K., 2012, Phys. Rev. D, 85, 083005
Springel V., Yoshida N., White S. D. M., 2001, New Astron., 6, 79
Springel V. et al., 2005, Nature, 435, 629
Springel V. et al., 2008, MNRAS, 391, 1685
Takahashi R., Oguri M., Sato M., Hamana T., 2011, ApJ, 742, 15
Vale C., White M., 2003, ApJ, 592, 699
Vegetti S., Koopmans L. V. E., Bolton A., Treu T., Gavazzi R., 2010, MNRAS, 408, 1969
Vegetti S., Lagattuta D. J., McKean J. P., Auger M. W., Fassnacht C. D., Koopmans L. V. E., 2012, Nature, 481, 341
Viel M., Becker G. D., Bolton J. S., Haehnelt M. G., 2013, Phys. Rev. D, 88, 043502
Wambsganss J., Cen R., Ostriker J. P., 1998, ApJ, 494, 29
Wang H. Y., Mo H. J., Jing Y. P., 2007, MNRAS, 375, 633
Xu D. D. et al., 2009, MNRAS, 398, 1235

This paper has been typeset from a TEX/LATEX file prepared by the author.

Downloaded from https://academic.oup.com/mnras/article/444/3/2925/1061679 by CNRS - ISTO user on 25 April 2022